

Mass and energy balance calculations for artificial ice reservoirs (Icestupas)

Suryanarayanan Balasubramanian^{1*}, Martin Hoelzle¹, Michael Lehning²,
Sonam Wangchuk³, Johannes Oerlemans⁴, Felix Keller^{5,6} and Jordi Bolíbar⁴

¹ University of Fribourg, Fribourg, Switzerland

² WSL Institute for Snow and Avalanche Research, Davos, Switzerland

³ Himalayan Institute of Alternatives Ladakh, Leh, India

⁴ Institute for Marine and Atmospheric Research, Utrecht University, Utrecht, The Netherlands

⁵ Academia Engiadina, Samedan, Switzerland

⁶ ETH, Zürich, Switzerland

Correspondence*:

Suryanarayanan Balasubramanian

suryanarayanan.balasubramanian@unifr.ch

2 ABSTRACT

3 Artificial Ice Reservoirs (AIRs) can successfully store water during winter and release the water
4 during spring and summer. This makes them a reliable fresh water resource for irrigation in
5 dry environments. Several AIRs have been built but studies of their water storage capacity and
6 efficiency are scarce. This study models a cone-shaped AIR popularly called Icestupa. Processes
7 involved in the development and temporal evolution of an Icestupa are calculated by a physically-
8 based model using equations governing the heat transfer, vapour diffusion and transport of
9 water that undergoes phase changes. These processes were quantified using meteorological
10 data in conjunction with fountain spray information (mass input of an Icestupa) to estimate the
11 quantity of frozen, melted, evaporated and runoff water at a location called 'Eispalast' in Fribourg,
12 Switzerland. At this measurement site, an Icestupa was built for model validation purposes. The
13 model was further tested by performing a sensitivity and uncertainty study showing that the most
14 sensitive parameters are the ice emissivity and the temperature threshold used to determine
15 precipitation phase. Model calculations estimate that the Eispalast Icestupa stored about 6% of
16 the total water sprayed as ice. In addition, we found that reducing nozzle diameter of the fountain
17 from 5 mm to 3 mm increases the water storage up to 78% without compromising on the storage
18 duration.

19 **Keywords:** iceshelf, mass balance, water storage, climate change adaptation, geoengineering

1 INTRODUCTION

20 Seasonal snow cover, glaciers and permafrost are expected to change their water storage capacity due
21 to climate change with major consequences for downriver water supply (Immerzeel et al., 2019). The
22 challenges brought about by these changes are especially important for dry mountain environments such as
23 in Central Asia or the Andes, which directly rely on the seasonal meltwater for their farming and drinking
24 needs (Hoelzle et al., 2019; Apel et al., 2018; Buytaert et al., 2017; Chen et al., 2016; Unger-Shayesteh



Figure 1. Icestupa in Ladakh, India on March 2017 was 24 m tall and contained around 3700 m³ of water. Picture Credits: Lobzang Dadul

25 et al., 2013). Some villages in Ladakh, India have already been forced to relocate due to glacial retreat and
26 the corresponding loss of their main fresh water resources (Grossman, 2015).

27 Artificial ice reservoirs (AIRs) have been considered to be a feasible way to adapt to these changes (Hock
28 et al., 2019; Nüsser et al., 2019b). An AIR is a human-made ice structure typically constructed during the
29 cold winter months and designed to slowly release freshwater during the warm and dry spring and summer
30 months. The main purpose of AIRs is irrigation. Therefore, AIRs are designed to store water in the form of
31 ice as long into the summer as possible. The energy required to construct an AIR is usually derived from
32 the gravitational head of the source water body. Some are constructed horizontally by freezing water using
33 a series of checkdams and others are built vertically by spraying water through fountain systems (Nüsser
34 et al., 2019a). The latter are colloquially referred to as Icestupas and are the subject of this study.

35 A typical Icestupa just requires a pipeline attached to a vertically mounted metal pipe with a fountain
36 nozzle for construction. Their water source is usually a high altitude lake or glacial stream. Due to the
37 altitude difference between the pipeline input and fountain output, water ejects from the fountain nozzle as
38 droplets that eventually lose their latent heat to the atmosphere and accumulate as ice around the metal pipe.
39 The fountain nozzle is raised through addition of further pipes as and when significant ice accumulates.
40 Typically, a dome of branches is constructed around the metal pipe so that such pipe extensions can be
41 done from within this dome. During the winter, the fountain is manually activated from sunset to sunrise.
42 Threads, tree branches and fishing nets are used to guide and accelerate the ice formation.

43 Since their invention in 2013 (Wangchuk, 2014), Icestupas have gained widespread publicity in the region
44 of Ladakh, Northern India since they require very little infrastructure, skills and energy to be constructed
45 in comparison to other water storage technologies. Compared to other AIR geometries, Icestupas (Fig.
46 1) can be built at lower altitudes and last much longer into the summer than other types of ice structures
47 (Wangchuk, 2014). However, to date, no reliable estimates exist about the amount of sprayed water that
48 is necessary to create them and the meltwater they provide (Nüsser et al., 2019a). Rough estimates of
49 Icestupa meltwater in Ladakh suggest that the water loss during the construction process is considerable
50 (see Appendix 6.1). A complete set of measurements of the water storage and energy balance are required
51 to understand the cause of the water losses better and increase the construction efficiency.

52 In this paper, we aim to develop a physically-based model of a vertical AIR (or Icestupa) that can quantify
53 their storage efficiency using existing weather and water usage information. Mass and energy balance
54 equations were used to estimate the quantity of water frozen, melted, evaporated and runoff. Sensitivity
55 and uncertainty analysis were performed to identify the most critical parameters and the variance caused
56 by them. For validation, we created an Icestupa at an accessible site (called Eispalast) near Schwarzsee
57 close to the city of Fribourg, Switzerland, allowing easy maintenance and control of the measurements.
58 Due to the low altitude of the site with relatively high winter temperatures, only a small Icestupa could
59 be established during winter 2018/19 to provide us with model validation data. Our model and validation
60 experiments provide first steps towards evaluating the effectiveness of a vertical AIR for irrigation and
61 allow us to outline some preliminary guidelines for consideration when a construction of an Icestupa for
62 water storage is envisaged.

2 STUDY SITES

63 To accurately estimate and validate the ice volume of AIR the model requires three kinds of datasets
64 namely, weather, water and ice volume. So through the winters of 2019, 2020 and 2021 several scientific
65 AIR were constructed by teams in Switzerland and India. Each site had an Automatic Weather Station
66 (AWS) nearby. Also drone flights were conducted periodically to record AIR ice volume. For this analysis,
67 we have chosen 4 of the AIR which have a relatively complete dataset associated with them.

68 2.1 Construction

69 The construction strategy used in each site varied. CH20 and CH21 AIR was constructed on a garden
70 adjacent to a stream. To initiate the ice formation process, tree branches were laid covering the fountain
71 pipe. The fountain height varied between 2 to 5 m during the construction period. Fountain operation was
72 guided by temperature conditions.

73 The IC21 AIR was constructed adjacent to another AIR and merged with it. To initiate the ice formation
74 process, a dome of 2 m radius was constructed and the fountain pipeline was erected at the center using a
75 tripod. Fountain operation was interrupted only due to pipeline freezing events. The fountain height varied
76 between 5 to 9 m.

77 The EP19 AIR was constructed inside a wooden boundary adjacent to a stream. Fountain operation was
78 guided by temperature conditions. The water spray of the fountain was initially adjusted so that most of
79 the water droplets land within the wooden boundary zone. The ice formation was guided by adding a
80 metal framework at the ice structure base after the first night of operation. Several cotton threads were tied
81 between the ice structure base and fountain pole for accelerating and further guiding the ice formation
82 process.

83 2.2 Measurements

84 2.2.1 Weather measurements

85 Air temperature, relative humidity, wind speed, pressure, longwave, shortwave direct and diffuse radiation
86 are required to calculate the surface energy balance of an AIR. All the 4 sites had AWS near the construction
87 site which measured most of these parameters. The specific corrections applied on the input dataset for
88 each site is described in the Appendix. In addition, we used ERA5 reanalysis dataset (Copernicus Climate
89 Change Service (C3S), 2017) for filling data gaps and adding data that were not measured directly at the
90 respective site. The ERA5 reanalysis dataset has a good correlation with lower elevation sites in Switzerland
91 (Scherrer, 2020) but a poor correlation for the Indian (IN21) site. So the weather dataset for the IN21 site
92 was completed using another AWS nearby as described in the Appendix.

93 2.2.2 Discharge measurements

94 The water flow rate or discharge was measured via an ultrasonic sensor attached to the fountain
 95 supply pipeline for all the sites. However, due to various malfunctions, the discharge measurements
 96 were incomplete for all the sites except CH19. Using the hourly webcam images of the CH sites, the
 97 discharge duration was determined. The available discharge measurement was later used to determine the
 98 average discharge quantity during these periods.

99 2.2.3 Ice volume measurements

100 Several Drone flights were conducted in every AIR site. The DEM generated through these flights were
 101 analysed to obtain the circumference and volume of the ice structure. The mean circumference measured
 102 during the fountain duration was set as the spray radius (r_{spray}) and the first drone flight was used to set
 103 the dome volume (V_{dome}) for model initialisation. The ice volume data was later used for calibration and
 104 validation of the model. There were no drone flights conducted for CH19 AIR, so the r_{spray} was instead
 105 calculated from fountain attributes as described in Appendix.

106

AIR	Gangles, 2021	Guttannen, 2021	Guttannen, 2020	Schwarzsee, 2019
Code	IN21	CH21	CH20	CH19
Altitude [m a.s.l.]	4025	1047	1047	967
Construction Team	Icestupa Competition	Guttannen Bewegt	Guttannen Bewegt	Eispalast
Fountain Duration	Jan 18 - Mar 10	Nov 22 - Feb 21	Jan 3 - Feb 27	Jan 30 - Feb 16
Drone Flights	6	9	3	0
r_{spray} [m]	10.8	6.9	7.7	1.2
V_{dome} [m^3]	78.5	13.2	23.9	0

108

The model application is restricted to CH21 AIR below. Model results and figures for other AIR can be
 109 found in the supplementary materials.

3 MODEL SETUP

110

A bulk energy and mass balance model is used to calculate the amounts of ice, meltwater, water vapour
 111 and runoff water of the AIR every hour. This model consists of four modules which estimates the AIR, a)
 112 geometric evolution , b) energy balance, c) surface temperature and d) mass balance.

113

3.1 Geometric evolution

114

Radius r_{ice}^i and height h_{ice}^i define the dimensions of the AIR assuming its geometry to be a cone. The
 115 surface area A^i exposed to the atmosphere and volume V^i are:

$$A = \pi \cdot r_{ice} \cdot \sqrt{r_{ice}^2 + h_{ice}^2} \quad (1)$$

$$V = \pi/3 \cdot r_{ice}^2 \cdot h_{ice} \quad (2)$$

116

Note that we do not specify the time step superscript i of the shape variables A , V , r_{ice} and h_{ice} for
 117 brevity. The equations used henceforth display model time step superscript i only if it is different from the
 118 current time step.

119

With the mass of the AIR M_{ice} , its current volume can also be expressed as:

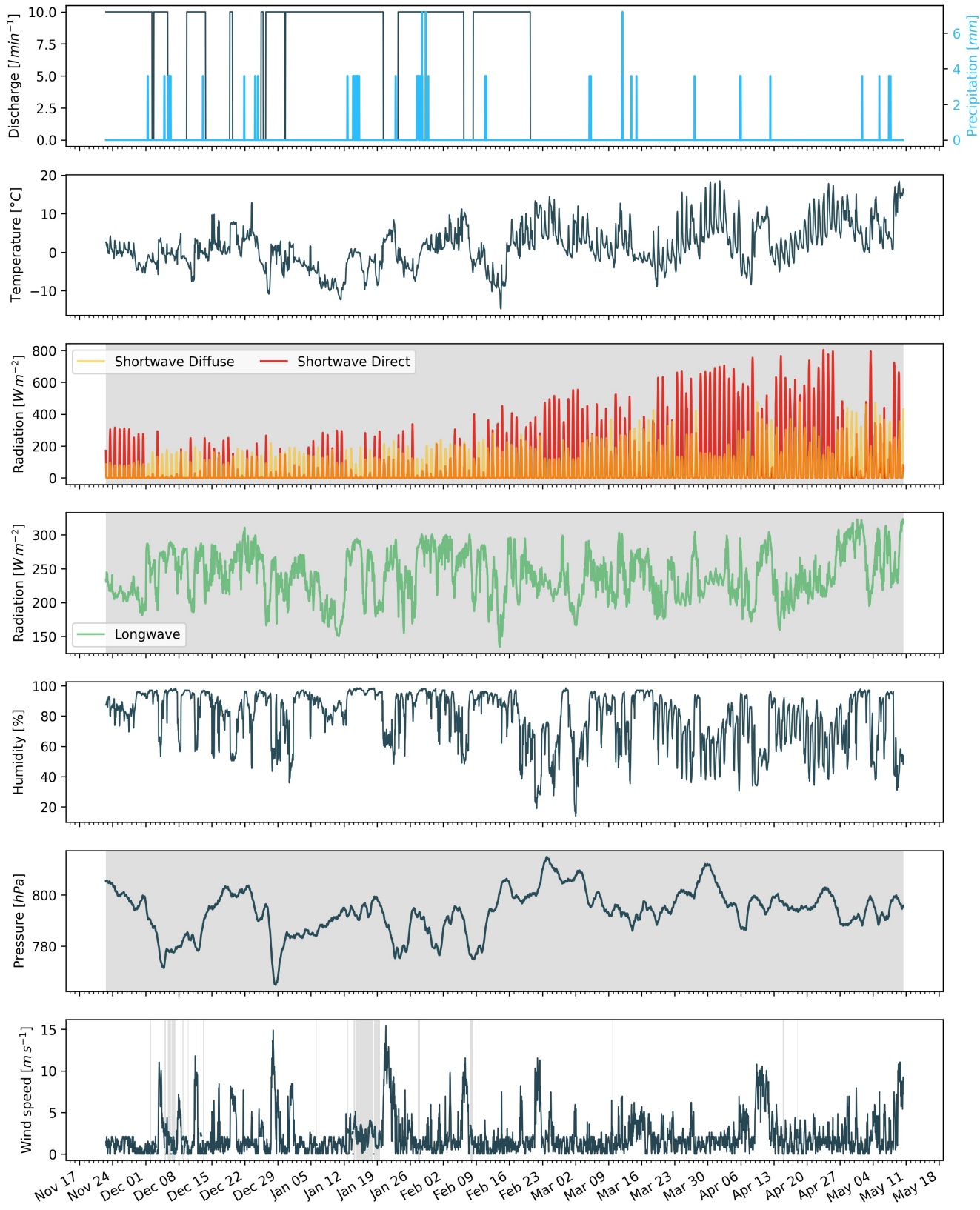


Figure 2. Measurements at the AWS of CH21 were used as main model input data in hourly frequency. Missing data, data gaps and errors were filled from the ERA5 dataset (shaded regions).

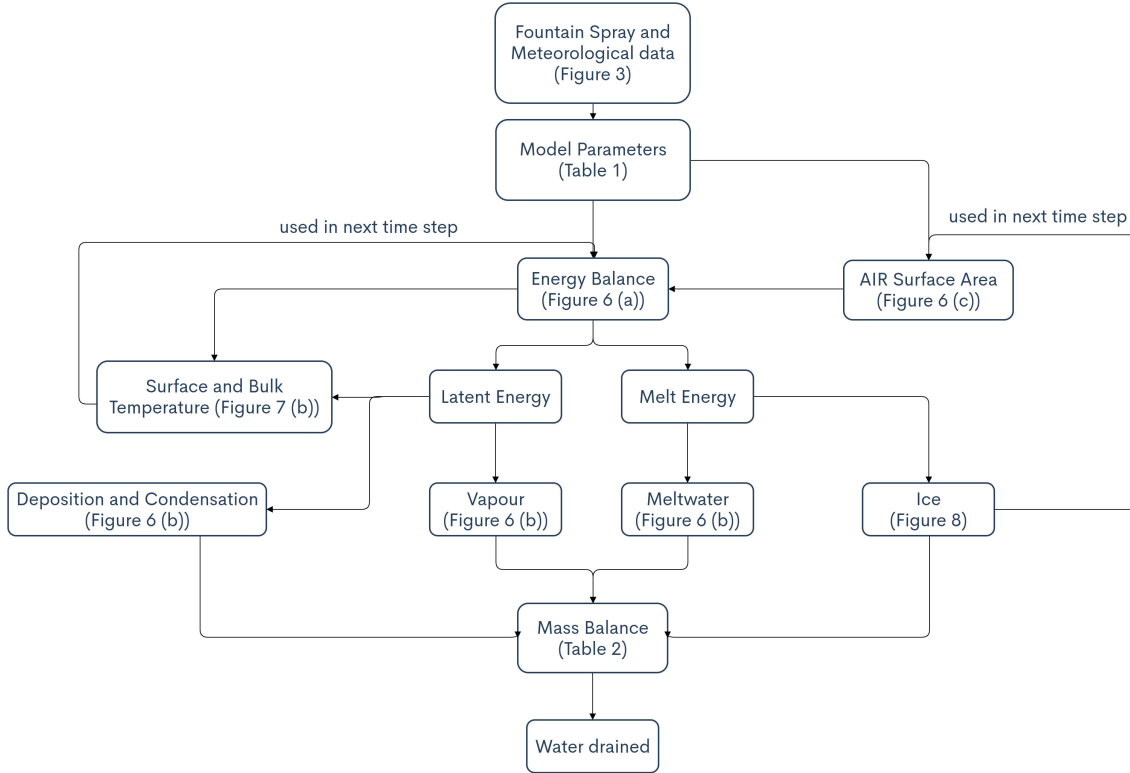


Figure 3. Model schematic showing the algorithm used in the model at every time step. Further details about the variables can be found in the associated tables and figures.

$$V = M_{ice} / \rho_{ice} \quad (3)$$

120 where ρ_{ice} is the density of ice (917 kg m^{-3}).

121 The influence of the AIR fountain is parameterised by the fountain water temperature T_w and its spray
122 radius r_{spray} . The initial radius r_0 of the AIR is assumed to be r_{spray} . The initial height h_0 depends on the
123 dome volume V_{dome} used to construct the AIR as follows:

$$h_0 = \Delta x + \frac{3 \cdot V_{dome}}{\pi r_{spray}^2} \quad (4)$$

124 where Δx is the surface layer thickness (defined in Section 3.2)

125 During subsequent time steps, the dimensions of the AIR evolve assuming a uniform ice formation and
126 decay across its surface area with an invariant slope $s_{cone} = \frac{h_{ice}}{r_{ice}}$. During these time steps, the volume is
127 parameterised using Eqn. 2 as:

$$V = \frac{\pi \cdot r_{ice}^3 \cdot s_{cone}}{3} \quad (5)$$

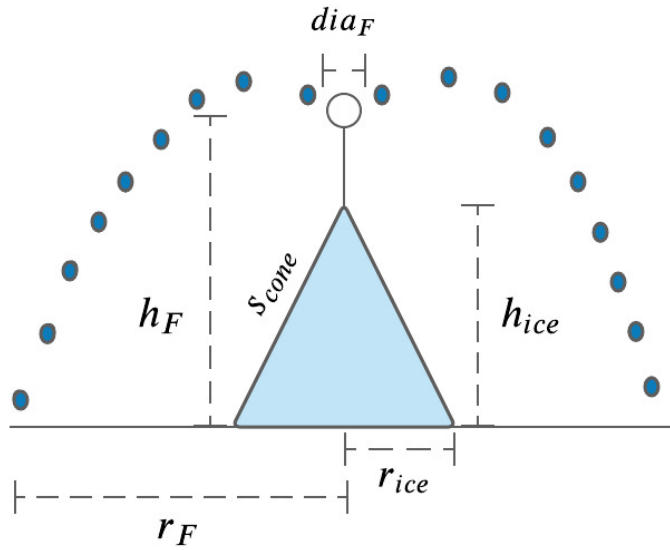


Figure 4. Shape variables and fountain constants of the CH21 Icestupa. r_{ice} is the radius, h_{ice} is the height and s_{cone} is the slope of the ice cone. r_{spray} is the spray radius, h_F is the height and dia_F is the nozzle diameter of the fountain.

128 However, the Icestupa cannot outgrow the maximum range of the water droplets ($(r_{ice})_{max} = r_F$).
 129 Combining equations 2, 4, 3 and 5, the geometric evolution of the Icestupa at each time step i can be
 130 determined by considering the following rules:

$$(r_{ice}, h_{ice}) = \begin{cases} (r_{spray}, h_0) & \text{if } i = 0 \\ (r_{ice}^{i-1}, \frac{3 \cdot M_{ice}}{\pi \cdot \rho_{ice} \cdot (r_{ice}^{i-1})^2}) & \text{if } r_{ice}^{i-1} \geq r_F \text{ and } \Delta M_{ice} > 0 \\ (\frac{3 \cdot M_{ice}}{\pi \cdot \rho_{ice} \cdot s_{cone}})^{1/3} \cdot (1, s_{cone}) & \text{otherwise} \end{cases} \quad (6)$$

131 where $\Delta M_{ice} = M_{ice}^{i-1} - M_{ice}^{i-2}$

132 3.2 Energy Balance

133 The energy balance equation (Hock, 2005) for the AIR is formulated as follows:

$$q_{SW} + q_{LW} + q_L + q_S + q_F + q_G = q_{surf} \quad (7)$$

134 where q_{surf} is the surface energy flux in $[W m^{-2}]$; q_{SW} is the net shortwave radiation; q_{LW} is the net
 135 longwave radiation; q_L and q_S are the turbulent latent and sensible heat fluxes. q_F represents the heat
 136 exchange of the fountain water droplets with the AIR ice surface. q_G represents ground heat flux between
 137 Icestupa surface and Icestupa interior. Energy transferred in the direction of the ice surface is always
 138 denoted as positive and away as negative.

139 Equation 7 is usually referred to as the energy budget for “the surface”, but practically it must apply
 140 to a surface layer of ice with a finite thickness Δx . The energy flux acts upon the Icestupa surface layer
 141 which has an upper and a lower boundary defined by the atmosphere and the ice body of the Icestupa,
 142 respectively. The parameter selection for Δx is based on the following two arguments: (a) the ice thickness

143 Δx should be small enough to represent the surface temperature variations every model time step Δt and
 144 (b) Δx should be large enough for these temperature variations to not reach the bottom of the surface layer.
 145 Therefore, we introduced a 20 mm thick surface layer for a model time step of 1 hour, over which the
 146 energy balance is calculated. A sensitivity analysis was later performed to understand the influence of this
 147 factor. Here, we define the surface temperature T_{ice} to be the modelled average temperature of the Icestupa
 148 surface layer and the energy flux q_{surf} is assumed to act uniformly across the Icestupa area A .

149 3.2.1 Net Shortwave Radiation q_{SW}

150 The net shortwave radiation q_{SW} is computed as follows:

$$151 \quad q_{SW} = (1 - \alpha) \cdot (SW_{direct} \cdot f_{cone} + SW_{diffuse}) \quad (8)$$

151 where SW_{direct} and $SW_{diffuse}$ are the ERA5 direct and diffuse short wave radiation, α is the modelled
 152 albedo and f_{cone} is the area fraction of the ice structure exposed to the direct shortwave radiation.

153 We model the albedo using a scheme described in Oerlemans and Knap (1998). The scheme records the
 154 decay of albedo with time after fresh snow is deposited on the surface. δt records the number of time steps
 155 after the last snowfall event. After snowfall, albedo changes over a time step, δt , as

$$\alpha = \alpha_{ice} + (\alpha_{snow} - \alpha_{ice}) \cdot e^{(-\delta t)/\tau} \quad (9)$$

156 where α_{ice} is the bare ice albedo value (0.35), α_{snow} is the snow ice albedo value (0.85) and τ is a decay
 157 rate, which determines how fast the albedo of the ageing snow reaches this value. The decay rate τ is
 158 assumed to have a base value of 10 days similar to values obtained by Schmidt et al. (2017) for wet surfaces
 159 and its maximal value is set based on observations by Oerlemans and Knap (1998) as shown in Table 1.
 160 Furthermore, the albedo α varies depending on the water source that formed the current Icestupa surface.
 161 Correspondingly, the albedo is reset to the value of bare ice albedo if the fountain is spraying water onto
 162 the current ice surface and to the value of fresh snow albedo if a snowfall event occurred. Snowfall events
 163 are assumed if the air temperature is below $T_{ppt} = 1^{\circ}C$ (Fujita and Ageta, 2000).

164 The area fraction f_{cone} of the ice structure exposed to the direct shortwave radiation depends on the
 165 shape considered. The direct solar radiation incident on the AIR surface is first decomposed into horizontal
 166 and vertical components using the solar elevation angle θ_{sun} . For a conical shape, half of the total curved
 167 surface is exposed to the vertical component of the direct shortwave radiation and the projected triangle
 168 of the curved surface is exposed to the horizontal component of the direct shortwave radiation. The solar
 169 elevation angle θ_{sun} used is modelled using the parametrisation proposed by Woolf (1968). Accordingly,
 170 f_{cone} is determined as follows:

$$171 \quad f_{cone} = \frac{(0.5 \cdot r_{ice} \cdot h_{ice}) \cdot \cos\theta_{sun} + (\pi \cdot r_{ice}^2 / 2) \cdot \sin\theta_{sun}}{\pi \cdot r_{ice} \cdot (r_{ice}^2 + h_{ice}^2)^{1/2}} \quad (10)$$

171 The ERA5 diffuse shortwave radiation is assumed to impact the conical Icestupa surface uniformly.

172 3.2.2 Net Longwave Radiation q_{LW}

173 The net longwave radiation q_{LW} is determined as follows:

$$q_{LW} = LW_{in} - \sigma \cdot \epsilon_{ice} \cdot (T_{ice} + 273.15)^4 \quad (11)$$

174 where T_a represents the measured air temperature, T_{ice} is the modelled surface temperature, both
 175 temperatures are given in $^{\circ}\text{C}$, $\sigma = 5.67 \cdot 10^{-8} \text{ J m}^{-2} \text{ s}^{-1} \text{ K}^{-4}$ is the Stefan-Boltzmann constant, LW_{in}
 176 denotes the incoming longwave radiation derived from the ERA5 dataset and ϵ_{ice} is the corresponding
 177 emissivity value for the Icestupa surface (see Table 1).

178 3.2.3 Turbulent sensible q_S and latent q_L heat fluxes

179 The turbulent sensible q_S and latent heat q_L fluxes are computed with the following expressions proposed
 180 by Garratt (1992):

$$q_S = c_a \cdot \rho_a \cdot p_a / p_{0,a} \cdot \frac{\kappa^2 \cdot v_a \cdot (T_a - T_{ice})}{(\ln \frac{h_{AWS}}{z_{ice}})^2} \quad (12)$$

$$q_L = 0.623 \cdot L_s \cdot \rho_a / p_{0,a} \cdot \frac{\kappa^2 \cdot v_a (p_{v,a} - p_{v,ice})}{(\ln \frac{h_{AWS}}{z_{ice}})^2} \quad (13)$$

181 where h_{AWS} is the measurement height above the ground surface of the AWS (in m), v_a is the wind
 182 speed in $[m \text{ s}^{-1}]$, c_a is the specific heat of air at constant pressure ($1010 \text{ J kg}^{-1} \text{ K}^{-1}$), ρ_a is the air density
 183 at standard sea level (1.29 kg m^{-3}), $p_{0,a}$ is the air pressure at standard sea level (1013 hPa), κ is the
 184 von Karman constant (0.4), L_s is the heat of sublimation (2848 kJ kg^{-1}) and z_{ice} (1.7 mm) denotes the
 185 roughness length of ice (momentum and scalar). The vapor pressures over air ($p_{v,a}$) and ice ($p_{v,ice}$) was
 186 obtained using the following formulation given in WMO (2018):

$$\begin{aligned} p_{v,a} &= 6.107 \cdot 10^{(7.5 \cdot T_a / (T_a + 237.3))} \\ p_{v,ice} &= (1.0016 + 3.15 \cdot 10^{-6} \cdot p_a - 0.074 \cdot p_a^{-1}) \cdot (6.112 \cdot e^{(22.46 \cdot T_{ice} / (T_{ice} + 272.62))}) \end{aligned} \quad (14)$$

187 where p_a is the measured air pressure in [hPa].

188 3.2.4 Fountain water heat flux q_F

189 The interaction between the fountain water and the ice surface is taken into account by assuming that
 190 the ice surface temperature remains constant at $0 \text{ }^{\circ}\text{C}$ during time steps when the fountain is active. This
 191 process can be divided into two simultaneous steps: (a) the water temperature T_{water} is cooled to $0 \text{ }^{\circ}\text{C}$
 192 and (b) the ice surface temperature is warmed to $0 \text{ }^{\circ}\text{C}$. Process (a) transfers the necessary energy for
 193 process (b) throughout the fountain runtime. We further assume that this process is instantaneous, i.e. the
 194 ice temperature is immediately set to $0 \text{ }^{\circ}\text{C}$ within just one time step Δt when the fountain is switched on.
 195 Thus, the heat flux caused by the fountain water is calculated as follows:

$$q_F = \begin{cases} 0 & \text{if } \Delta M_F = 0 \\ \frac{\Delta M_F \cdot c_{water} \cdot T_{water}}{\Delta t \cdot A} + \frac{\rho_{ice} \cdot \Delta x \cdot c_{ice} \cdot T_{ice}}{\Delta t} & \text{if } \Delta M_F > 0 \end{cases} \quad (15)$$

196 with c_{ice} as the specific heat of ice.

197 3.2.5 Bulk Icestupa heat flux q_G

198 The bulk Icestupa heat flux q_G corresponds to the ground heat flux in normal soils and is caused by the
 199 temperature gradient between the surface layer (T_{ice}) and the ice body (T_{bulk}). It is expressed by using the
 200 heat conduction equation as follows:

$$q_G = k_{ice} \cdot (T_{bulk} - T_{ice}) / l_{ice} \quad (16)$$

201 where k_{ice} is the thermal conductivity of ice ($2.123 \text{ W m}^{-1} \text{ K}^{-1}$), T_{bulk} is the mean temperature of the
 202 ice body within the Icestupa and l_{ice} is the average distance of any point in the surface to any other point in
 203 the ice body. T_{bulk} is initialised as 0°C and later determined from Eqn. 16 as follows:

$$T_{bulk}^{i+1} = T_{bulk} - (q_G \cdot A \cdot \Delta t) / (M_{ice} \cdot c_{ice}) \quad (17)$$

204 Since AIR's typically have conical shapes with $r_{ice} \gg h_{ice}$, we assume that the center of mass of the ice
 205 body is near the base of the fountain. Thus, the distance of every point in the AIR surface layer from the ice
 206 body's center of mass is between h_{ice} and r_{ice} . So we calculate q_G here assuming $l_{ice} = (r_{ice} + h_{ice})/2$.

207 3.3 Surface temperature

208 The available energy q_{surf} can act on the surface of the AIR to a) change its temperature, b) melt ice or
 209 c) freeze ice. So Eqn. 7 can be rewritten as:

$$q_{surf} = q_{freeze/melt} + q_T \quad (18)$$

210 where q_T , q_{freeze} and q_{melt} represent energy associated with process (a), (b) and (c) respectively.

211 To distribute the surface energy flux into these three components, we categorize the model time steps
 212 as freezing or melting events. Freezing events can only occur if there is fountain water available and the
 213 surface energy flux is negative. But just these two conditions are not sufficient as the latent heat energy
 214 can only contribute to temperature fluctuations. So to prevent latent heat energy from turning a melting
 215 event into a freezing event an additional condition namely $(q_{surf} - q_L) < 0$ is required. Thus, freezing and
 216 melting events are identified as follows:

$$q_{freeze/melt} = \begin{cases} q_{freeze} & \text{if } \Delta M_F > 0 \text{ and } q_{surf} < 0 \text{ and } (q_{surf} - q_L) < 0 \\ q_{melt} & \text{otherwise} \end{cases} \quad (19)$$

217 During a freezing event, the available energy $(q_{surf} - q_L)$ can either be sufficient or insufficient to
 218 freeze the fountain water available. If insufficient, the additional energy further cools down the surface
 219 temperature. So the surface energy flux distribution during a freezing event can be represented as:

$$(q_{freeze}, q_T) = \begin{cases} (q_{surf} - q_L, q_L) & \text{if } \Delta M_F \geq -\frac{(q_{surf} - q_L)A \cdot \Delta t}{L_f} \\ \left(\frac{\Delta M_F \cdot L_f}{A \cdot \Delta t}, q_{surf} + \frac{\Delta M_F \cdot L_f}{A \cdot \Delta t}\right) & \text{if } \Delta M_F < -\frac{(q_{surf} - q_L)A \cdot \Delta t}{L_f} \end{cases} \quad (20)$$

220 During a melting event, the surface energy flux (q_{surf}) is first used to change the surface temperature to
 221 T_{temp} calculated as:

Table 1. Free parameters in the model categorised as constant, uncertain and site parameters. Base value (B) and uncertainty (U) were taken from the literature. For assumptions (assum.), the uncertainty was chosen to be relatively large (5 %). For measurements (meas.), the uncertainty due to parallax errors is chosen to be (1 %).

Constant Parameters	Symbol	Value	References
Van Karman constant	κ	0.4	B: Cuffey and Paterson
Stefan Boltzmann constant	σ	$5.67 \cdot 10^{-8} W m^{-2} K^{-4}$	B: Cuffey and Paterson
Air pressure at sea level	$p_{0,a}$	1013 hPa	B: Mölg and Hardy
Density of water	ρ_w	$1000 kg m^{-3}$	B: Cuffey and Paterson
Density of ice	ρ_{ice}	$917 kg m^{-3}$	B: Cuffey and Paterson
Density of air	ρ_a	$1.29 kg m^{-3}$	B: Mölg and Hardy
Specific heat of ice	c_{ice}	$2097 J kg^{-1} ^\circ C^{-1}$	B: Cuffey and Paterson
Specific heat of water	c_w	$4186 J kg^{-1} ^\circ C^{-1}$	B: Cuffey and Paterson
Specific heat of air	c_a	$1010 J kg^{-1} ^\circ C^{-1}$	B: Mölg and Hardy
Thermal conductivity of ice	k_{ice}	$2.123 W m^{-1} K^{-1}$	B: Bonales et al.
Latent Heat of Sublimation	L_s	$2848 kJ kg^{-1}$	B: Cuffey and Paterson
Latent Heat of Fusion	L_f	$334 kJ kg^{-1}$	B: Cuffey and Paterson
Uncertain Parameters		Range	
Precipitation	T_{ppt}	$1 ^\circ C$	$\pm 1 ^\circ C$
Temperature threshold			B + U: Fujita and Ageta, Zhou et al.
Ice Emissivity	ϵ_{ice}	0.95	[0.949,0.993]
Ice Albedo	α_{ice}	0.35	$\pm 5 \%$
Snow Albedo	α_{snow}	0.85	$\pm 5 \%$
Albedo Decay Rate	τ	10 days	[1, 22] days
Surface layer thickness	Δx	20 mm	[1, 10] mm
Fountain Parameters		Range	
Spray Radius	r_{spray}		$\pm 5 \%$
Water temperature	T_{water}	$1 ^\circ C$	[0, 5] $^\circ C$

$$T_{temp} = \frac{q_{surf} \cdot \Delta t}{\rho_{ice} \cdot c_{ice} \cdot \Delta x} + T_{ice} \quad (21)$$

If $T_{temp} > 0^\circ C$, then energy is reallocated from q_T to q_{melt} to maintain surface temperature at melting point. So the surface energy flux distribution during a melting event can be represented as:

$$(q_{melt}, q_T) = \begin{cases} (0, q_{surf}) & \text{if } T_{temp} < 0 \\ \left(\frac{T_{temp} \cdot \rho_{ice} \cdot c_{ice} \cdot \Delta x}{\Delta t}, q_{surf} - \frac{T_{temp} \cdot \rho_{ice} \cdot c_{ice} \cdot \Delta x}{\Delta t} \right) & \text{if } T_{temp} > 0 \end{cases} \quad (22)$$

3.4 Mass Balance

The mass balance equation for an AIR is represented as:

$$\frac{\Delta M_F + \Delta M_{ppt} + \Delta M_{dep}}{\Delta t} = \frac{\Delta M_{ice} + \Delta M_{water} + \Delta M_{sub} + \Delta M_{runoff}}{\Delta t} \quad (23)$$

226 where M_F is the discharge of the fountain; M_{ppt} is the cumulative precipitation; M_{dep} is the cumulative
 227 accumulation through water vapour deposition; M_{ice} is the cumulative mass of ice; M_{water} is the cumulative
 228 mass of melt water; M_{sub} represents the cumulative water vapor loss by sublimation and M_{runoff} represents
 229 the fountain discharge runoff that did not interact with the AIR. The LHS of equation 23 represents the rate
 230 of mass input and the RHS represents the rate of mass output for an AIR.

231 Precipitation input is calculated as shown in equation 24a where ρ_w is the density of water (1000
 232 $kg\ m^{-3}$), ppt is the measured precipitation rate in [$m\ s^{-1}$] and T_{ppt} is the temperature threshold below
 233 which precipitation falls as snow. Here, snowfall events were identified using T_{ppt} as $1^{\circ}C$. Snow mass
 234 input is calculated by assuming a uniform deposition over the entire circular footprint of the Icestupa.

235 The latent heat flux is used to estimate either the evaporation and condensation processes or sublimation
 236 and deposition processes as shown in equation 24b. During time steps at which surface temperature is
 237 below $0^{\circ}C$ only sublimation and deposition can occur, but if the surface temperature reaches $0^{\circ}C$,
 238 evaporation and condensation can also occur. As the differentiation between evaporation and sublimation
 239 (and condensation and deposition) when the air temperature reaches $0^{\circ}C$ is challenging, we assume
 240 that negative (positive) latent heat fluxes correspond only to sublimation (deposition), i.e. no evaporation
 241 (condensation) is calculated.

242 Since we have categorized every time step as a freezing and melting event, we can determine the meltwater
 243 and ice generated using the associated energy fluxes as shown in equations 24c and 24d. Having calculated
 244 all the other mass components the fountain wastewater generated every time step can be calculated using
 245 equation 24e.

$$\frac{\Delta M_{ppt}}{\Delta t} = \begin{cases} \pi \cdot r_{ice}^2 \cdot \rho_w \cdot ppt & \text{if } T_a < T_{ppt} \\ 0 & \text{if } T_a \geq T_{ppt} \end{cases} \quad (24a)$$

$$\left(\frac{\Delta M_{dep}}{\Delta t}, \frac{\Delta M_{sub}}{\Delta t} \right) = \begin{cases} \frac{q_L \cdot A}{L_s} \cdot (1, 0) & \text{if } q_L \geq 0 \\ \frac{q_L \cdot A}{L_s} \cdot (0, -1) & \text{if } q_L < 0 \end{cases} \quad (24b)$$

$$\frac{\Delta M_{water}}{\Delta t} = \frac{q_{melt} \cdot A}{L_f} \quad (24c)$$

$$\frac{\Delta M_{ice}}{\Delta t} = \frac{q_{freeze} \cdot A}{L_f} + \frac{\Delta M_{ppt}}{\Delta t} + \frac{\Delta M_{dep}}{\Delta t} - \frac{\Delta M_{sub}}{\Delta t} - \frac{\Delta M_{melt}}{\Delta t} \quad (24d)$$

$$\frac{\Delta M_{runoff}}{\Delta t} = \frac{\Delta M_F - \Delta M_{ice}}{\Delta t} \quad (24e)$$

246 Considering AIRs as water reservoirs, we can quantify their potential through the amount of water they
 247 store (storage quantity) and the length of time they store it (storage duration). Another means of comparing
 248 different Icestupas is through their water storage efficiency defined accordingly as:

$$\text{Storage Efficiency} = \frac{M_{water}}{(M_F + M_{ppt} + M_{dep})} \cdot 100 \quad (25)$$

4 MODEL RESULTS

249 The model was forced with meteorological data from 22nd November to 10th May 2021 (Fig. 2) and
250 various parameters (see Table 1) to calculate the mass and energy balance of the CH21 AIR.

251 4.1 Energy and mass balance calculation

252 Daily averages of some components of the energy balance are shown in Fig. 5 (b). On average during
253 the experiment duration, the total energy balance was almost zero. Net shortwave radiation (35 W m^{-2}),
254 sensible (41 W m^{-2}) and latent heat flux (2 W m^{-2}) with a mostly positive flux towards the surface of the
255 icestupa were compensated by the net longwave radiation (- 47 W m^{-2}), the fountain water heat flux (-
256 13 W m^{-2}) and the freeze/melt energy (- 19 W m^{-2}). The contributions of other fluxes were negligible in
257 comparison.

258 Net shortwave radiation is the main input to, and the most varying energy flux on the ice surface. Its
259 variability is controlled by the surface albedo α and the area fraction f_{cone} which therefore represent key
260 variables in the energy balance (Fig. 6 (b)). Although global radiation flux reached a daily maximum value
261 of 340 W m^{-2} , q_{SW} only went up to 114 W m^{-2} . This is caused by the fact that less than 40 % of the direct
262 solar radiation influenced the Icestupa surface as shown by the area fraction f_{cone} in Fig. 6 (a). Snowfall is
263 the atmospheric variable connected most closely and proportionally to albedo. Higher and/or more frequent
264 snowfall thus decreases the energy available for melt due to the corresponding increase in α .

265 q_{LW} was predominantly negative indicating that this energy balance component drove the freezing of
266 the ice structure. Daily values of q_{LW} ranged from - 101 to 19 W m^{-2} . Turbulent sensible heat flux q_S
267 contributed mostly to the melt of the ice structure. Daily values of q_S ranged from - 3 to 410 W m^{-2} . Daily
268 values of the turbulent latent heat flux q_L ranged from - 90 to 157 W m^{-2} . Since the mean of q_L was positive,
269 the Icestupa gained mass cumulatively from the atmosphere due to the deposition process. Daily values
270 of fountain water heat flux ranged from - 119 to 4 W m^{-2} . q_F was also a significant contributor to the
271 freezing process like q_{LW} . So the influence of the fountain on the energy balance and the freezing events
272 was significant. The contribution of heat flux by conduction q_G was minimal as it only varied between
273 - 1 to 3 W m^{-2} with a mean of 0 W m^{-2} . The energy contributing to surface temperature changes (q_T)
274 was insignificant in comparison to the energy spent on freezing and melting ($q_{freeze/melt}$). The resulting
275 bulk temperature and the surface temperature are shown in Fig. 6 (b). For the total considered period,
276 $q_{freeze/melt}$ accounted for 30% of overall energy turnover. The energy turnover is calculated as the sum of
277 energy fluxes in absolute values. q_{LW} accounted for 22%, followed by q_S (20%), q_{SW} (16%), q_L (5%), q_F
278 (6%), q_T (1%) and q_G (0%).

279 Fig. 5 (c) represents the mass fluxes associated with these energy exchanges expressed in m w.e. It shows
280 the ice and meltwater formed due to q_{melt} , snow accumulated due to precipitation, water vapour deposition
281 and sublimation due to q_L .

282 The total water used for the Icestupa development includes contributions from the fountain (96.7%),
283 snowfall (2.9 %), deposition (0.5 %) as shown in Table 2. Therefore, in the case of CH21 we used a water
284 input of 1,034,328 kg, with a resultant storage efficiency of 19 %.

5 DISCUSSION

285 5.1 Important assumptions

286 In the sensitivity and uncertainty analysis presented above, we did not account for several general
287 assumptions and parametrisation choices that may cause model errors. Some assumptions and their
288 potential to cause errors are discussed below.

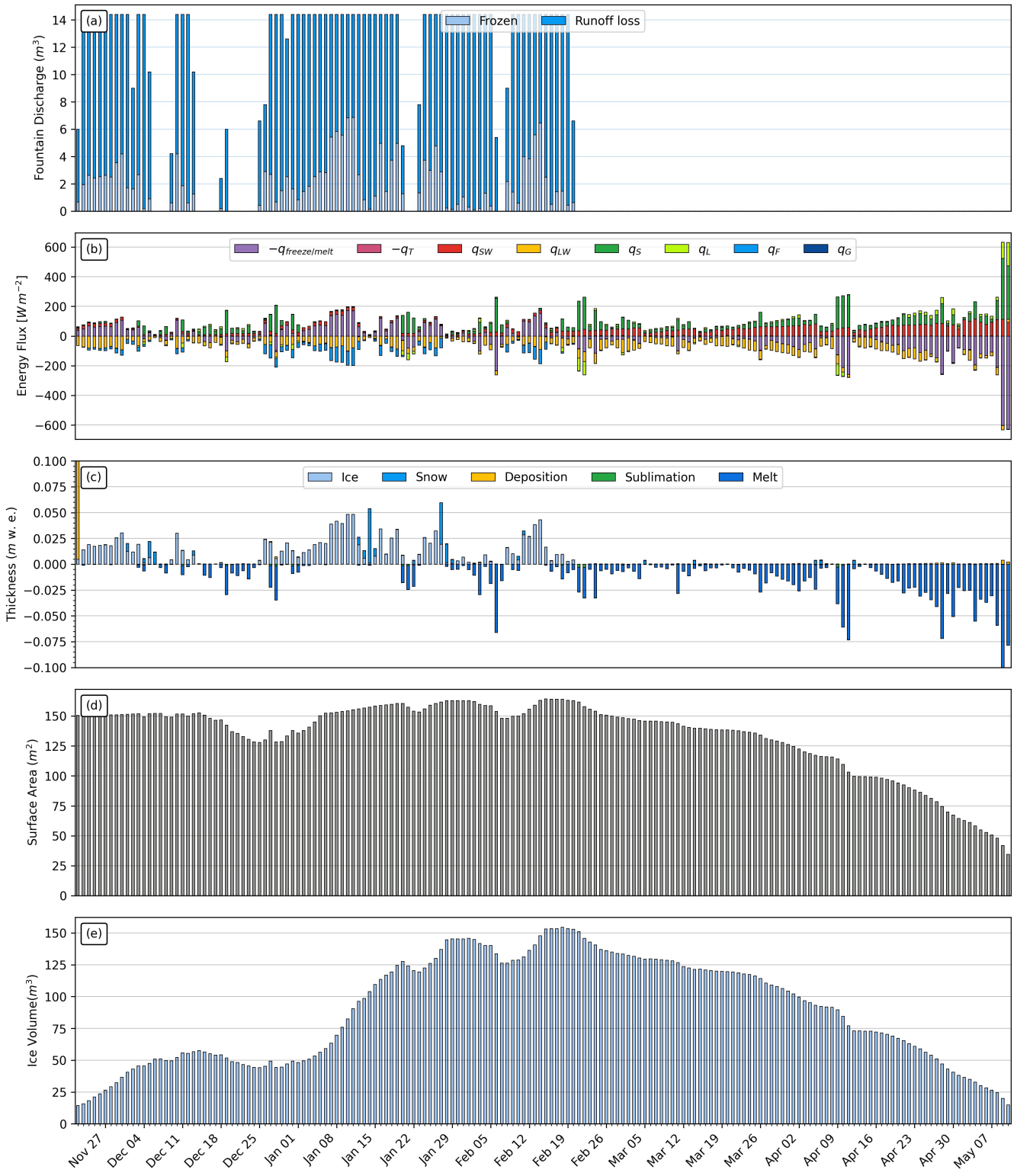


Figure 5. (a) Fountain discharge (b) energy flux components, (c) mass flux components (d) surface area and (e) volume of the Icestupa in daily time steps. q_{SW} is the net shortwave radiation; q_{LW} is the net longwave radiation; q_L and q_S are the turbulent latent and sensible heat fluxes. q_F represents the interactions of the fountain water with the AIR surface layer. q_G quantifies the heat conduction process between the AIR surface layer and the ice body.

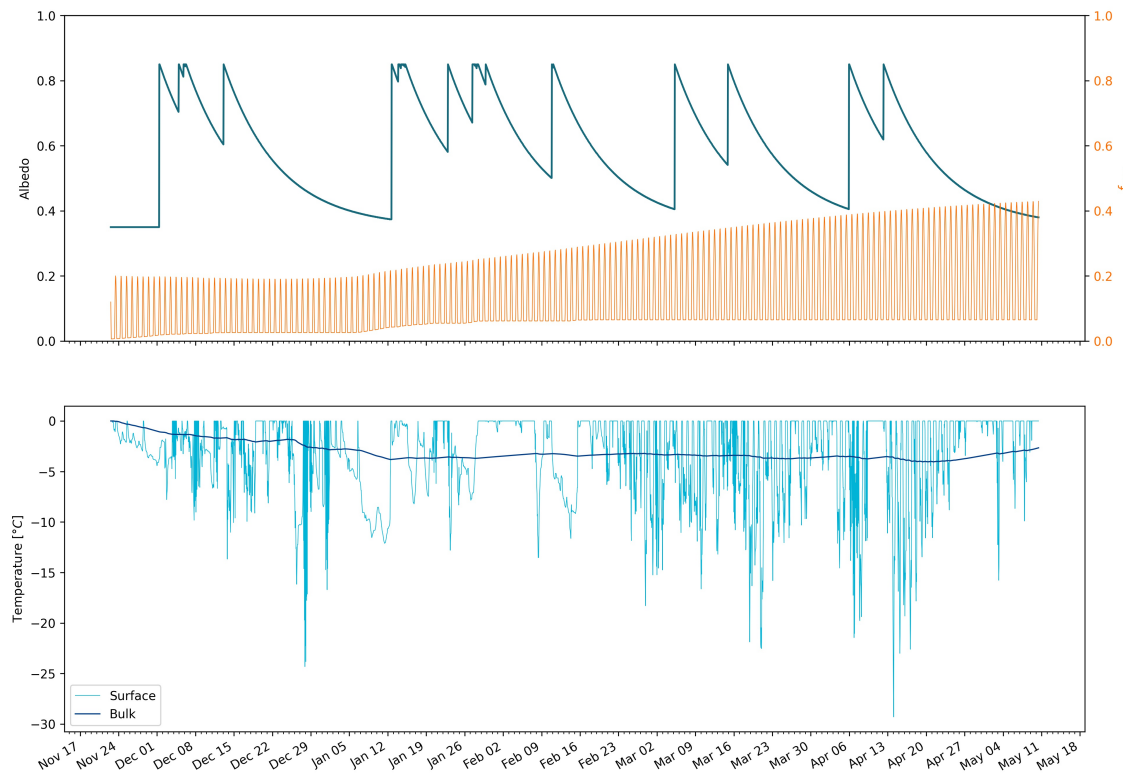


Figure 6. Some derived parameters of the model, namely, albedo and f_{cone} (a), Surface and bulk temperature (b). In (a), the green curve shows how snow and fountain-on events reset albedo between ice albedo and snow albedo. The decay of the snow albedo to ice albedo can also be observed. The orange curve shows how the solar radiation area fraction varied diurnally with variations in the solar elevation angle. In (b), the surface temperature (light blue curve) was forced to be 0°C during fountain activity. The corresponding bulk temperature is shown with the dark blue curve.

Table 2. Summary of mass balance components for the CH21 AIR at the end of the model run on 10th May 2021.

	Mass Component	Model ends
Input	M_F	1,000,041 kg
	M_{ppt}	29,533 kg
	M_{dep}	4,755 kg
Output	M_{water}	196,011 kg
	M_{ice}	12,304 kg
	M_{sub} M_{runoff}	4,747 kg 821,267 kg

- 289 • Turbulent Sensible and Latent Heat Fluxes: The method used to calculate the turbulent heat fluxes
 290 by Garratt (1992) assumes that the turbulent heat fluxes are acting over a uniform planar surface to
 291 determine the roughness length. Since our application is on a conical surface, the distance to the ice
 292 surface is not uniform and well defined. Hence, z_{ice} has no real physical significance here.

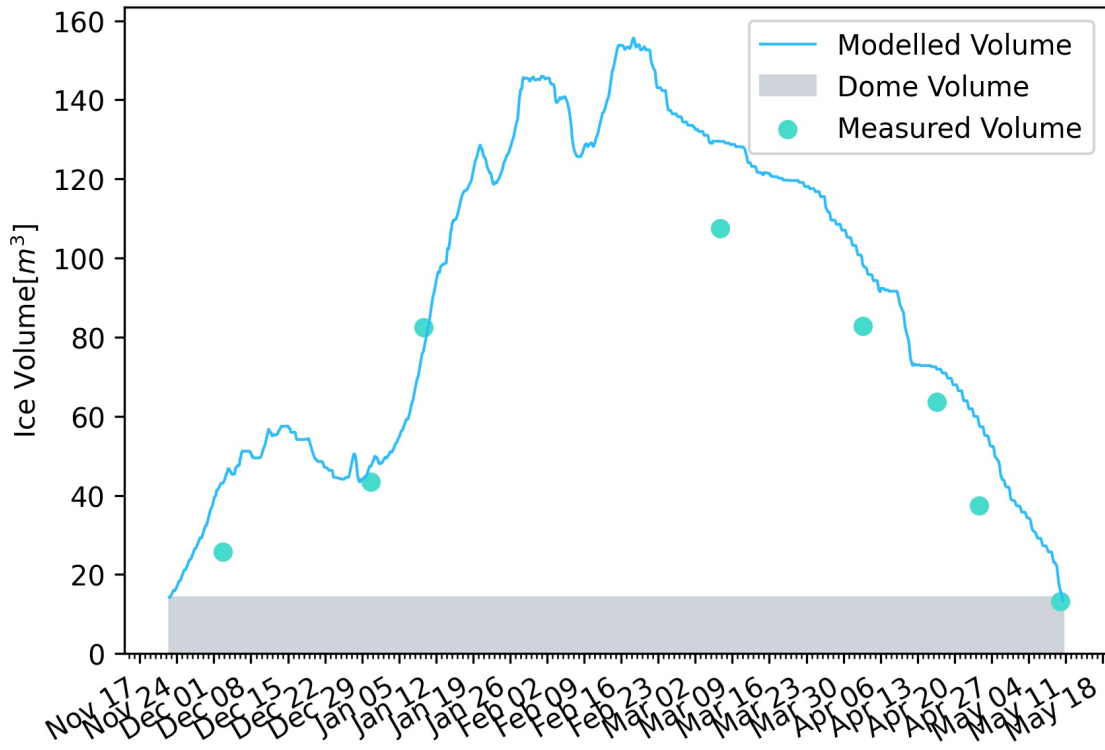


Figure 7. Modelled ice volume during the lifetime of the CH21 AIR (blue curve). Green points indicate the validation measurements.

- 293 • Droplet flight time loss: Water losses during the flight time of fountain droplets were neglected making
- 294 all the fountain spray available for freezing. For the CH21 experiment, inclusion of this parameter does
- 295 not influence results since it is already accounted for in the runoff water discharge rate which was at
- 296 least $3 l \text{ min}^{-1}$.
- 297 • Nucleation of droplets: Corresponding to droplet flight time, ice/snow formation is also possible before
- 298 surface contact if nucleation occurs during flight time. For the CH21 experiment, this process will
- 299 further increase the freeze rate and hence the storage efficiency. This process is neglected for model
- 300 simplicity.
- 301 • Shape Effects: The suppression of heat exchange between the snow/ice surface and the air adjacent
- 302 to the surface effectively slows down snow/ice ablation in spring and promotes the stagnation of the
- 303 cold air within topographical depressions (Fujita et al., 2010). The quantitative contribution of the
- 304 atmospheric decoupling over melting snow/ice for the total mass and energy balance is ignored in the
- 305 model.

6 APPENDIX

306 6.1 Ladakh Icestupa 2014/15

307 A 20 m tall Icestupa (Wangchuk, 2015c) was built in Phyang village, Ladakh at an altitude of 3500
 308 m a.s.l. Assuming a conical shape with a diameter of 20 m, the corresponding volume of this Icestupa
 309 becomes $2093 m^3$ or $1,920 m^3$ w.e. The fountain sprayed water at a rate of $210 l \text{ min}^{-1}$ (Wangchuk,
 310 2015e) from 21st January (Wangchuk, 2015a) to at least until 5th March 2015 (Wangchuk, 2015b) (around
 311 43 nights). Assuming fountain spray was active for 8 hours each night, we estimate water consumption to

312 be around $4,334\text{ m}^3$. Thus, during the construction/freezing period of the Icestupa, roughly 56 % of the
313 water provided was wasted. The actual water loss is bound to be much higher due to further vapour losses
314 during the melting period. This Icestupa completely melted away on 6th July 2015 (Wangchuk, 2015d).
315 Therefore, the storage duration was 166 days or roughly 5 months.

REFERENCES

- 316 Apel, H., Abdykerimova, Z., Agalhanova, M., Baimaganbetov, A., Gavrilenko, N., Gerlitz, L., et al. (2018).
317 Statistical forecast of seasonal discharge in central asia using observational records: development of a
318 generic linear modelling tool for operational water resource management. *Hydrology and Earth System
319 Sciences* 22, 2225–2254. doi:10.5194/hess-22-2225-2018
- 320 Bonales, L. J., Rodriguez, A. C., and Sanz, P. D. (2017). Thermal conductivity of ice prepared under
321 different conditions. *International Journal of Food Properties* 20, 610–619. doi:10.1080/10942912.
322 2017.1306551
- 323 Buytaert, W., Moulds, S., Acosta, L., Bievre, B. D., Olmos, C., Villacis, M., et al. (2017). Glacial melt
324 content of water use in the tropical andes. *Environmental Research Letters* 12, 114014. doi:10.1088/
325 1748-9326/aa926c
- 326 Chen, Y., Li, W., Deng, H., Fang, G., and Li, Z. (2016). Changes in central asia's water tower: Past, present
327 and future. *Nature* doi:10.1088/1748-9326/aa926c
- 328 [Dataset] Copernicus Climate Change Service (C3S) (2017). Era5: Fifth generation of ecmwf atmospheric
329 reanalyses of the global climate. [Available at [https://cds.climate.copernicus.eu/
330 cdsapp#!/home](https://cds.climate.copernicus.eu/cdsapp#!/home), accessed 2019-10-01]
- 331 Cuffey, K. M. and Paterson, W. S. B. (2010). *The Physics Of Glaciers* (Elsevier)
- 332 Fujita, K. and Ageta, Y. (2000). Effect of summer accumulation on glacier mass balance on the
333 tibetan plateau revealed by mass-balance model. *Journal of Glaciology* 46, 244–252. doi:10.3189/
334 172756500781832945
- 335 Fujita, K., Hiyama, K., Iida, H., and Ageta, Y. (2010). Self-regulated fluctuations in the ablation of a snow
336 patch over four decades. *Water Resources Research* 46, W11541. doi:10.1029/2009WR008383
- 337 Garratt, J. R. (1992). *The Atmospheric Boundary Layer* (Cambridge University Press)
- 338 Grossman, D. (2015). As himalayan glaciers melt, two towns face the fallout [Available at
339 [https://e360.yale.edu/features/as_himalayan_glaciers_melt_two_towns_
340 face_the_fallout](https://e360.yale.edu/features/as_himalayan_glaciers_melt_two_towns_face_the_fallout), accessed 2019-10-01]
- 341 Hock, R. (2005). Glacier melt: a review of processes and their modelling. *Progress in Physical Geography:
342 Earth and Environment* 29, 362–391
- 343 Hock, R., Rasul, G., Adler, C., Cáceres, B., Gruber, S., Hirabayashi, Y., et al. (2019). 2019: High mountain
344 areas. *IPCC Special Report on the Ocean and Cryosphere in a Changing Climate* [H.-O. Pörtner; D.C.
345 Roberts, V. Masson-Delmotte, P. Zhai, M. Tignor, E. Poloczanska, K. Mintenbeck, A. Alegria, M. Nicolai,
346 A. Okem, J. Petzold, B. Rama, N.M. Weyer (eds.)]
- 347 Hoelzle, M., Barandun, M., Bolch, T., Fiddes, J., Gafurov, A., Muccione, V., et al. (2019). *The status and
348 role of the alpine cryosphere in Central Asia*. doi:10.4324/9780429436475-8
- 349 Hori, M., Aoki, T., Tanikawa, T., Motoyoshi, H., Hachikubo, A., Sugiura, K., et al. (2006). In-situ
350 measured spectral directional emissivity of snow and ice in the 8–14 micrometer atmospheric window.
351 *Remote Sensing of Environment* 100, 486 – 502
- 352 Immerzeel, W. W., Lutz, A. F., Andrade, M., Bahl, A., Biemans, H., Bolch, T., et al. (2019). Importance
353 and vulnerability of the world's water towers. *Nature* 577, 364 – 369. doi:10.1038/s41586-019-1822-y

- 354 Mölg, T. and Hardy, D. R. (2004). Ablation and associated energy balance of a horizontal glacier surface
355 on kilimanjaro. *J. Geophys. Res.-Atmos.* 109, 1–13. doi:10.1029/2003JD004338
- 356 Nüsser, M., Dame, J., Kraus, B., Baghel, R., and Schmidt, S. (2019a). Socio-hydrology of artificial glaciers
357 in ladakh, india: assessing adaptive strategies in a changing cryosphere. *Regional Environmental Change*
358 doi:10.1007/s10113-018-1372-0
- 359 Nüsser, M., Dame, J., Parveen, S., Kraus, B., Baghel, R., and Schmidt, S. (2019b). Cryosphere-Fed
360 Irrigation Networks in the Northwestern Himalaya: Precarious Livelihoods and Adaptation Strategies
361 Under the Impact of Climate Change. *Mountain Research and Development* 39. doi:10.1659/
362 MRD-JOURNAL-D-18-00072.1
- 363 Oerlemans, J. and Knap, W. H. (1998). A 1 year record of global radiation and albedo in the
364 ablation zone of morteratschgletscher, switzerland. *Journal of Glaciology* 44, 231–238. doi:10.
365 3189/S0022143000002574
- 366 Scherrer, S. C. (2020). Temperature monitoring in mountain regions using reanalyses: lessons from the
367 alps. *Environmental Research Letters* 15, 044005
- 368 Schmidt, L. S., Aðalgeirs Þóttir, G., Guðmundsson, S., Langen, P. L., Pálsson, F., Mottram, R., et al. (2017).
369 The importance of accurate glacier albedo for estimates of surface mass balance on vatnajökull: evaluating
370 the surface energy budget in a regional climate model with automatic weather station observations. *The
371 Cryosphere* 11, 1665–1684. doi:10.5194/tc-11-1665-2017
- 372 Unger-Shayesteh, K., Vorogushyn, S., Farinotti, D., Gafurov, A., Duethmann, D., Mandychev, A., et al.
373 (2013). What do we know about past changes in the water cycle of central asian headwaters? a review.
374 *Global and Planetary Change* 110, 4 – 25. doi:10.1016/j.gloplacha.2013.02.004. Water in Central Asia
375 – Perspectives under global change
- 376 Wangchuk, S. (2014). Ice stupa artificial glaciers of ladakh [Available at www.indiegogo.com/projects/ice-stupa-artificial-glaciers-of-ladakh#/, accessed 2019-10-01]
- 377 Wangchuk, S. (2015a). The good news at ice stupa 24th january 2015 [Available at <http://icestupa.org/news/the-good-news-at-ice-stupa>, accessed 2019-10-01]
- 378 Wangchuk, S. (2015b). Ice stupa artificial glacier inaugurated
379 5th of march 2015 [Available at <http://icestupa.org/news/ice-stupa-artificial-glacier-inaugurated-5th-of-march>, accessed
380 2019-10-01]
- 381 Wangchuk, S. (2015c). Ice stupa surpasses guiness world record [Available at <http://icestupa.org/news/ice-stupa-surpasses-guinness-world-record>, accessed 2019-10-01]
- 382 Wangchuk, S. (2015d). Ice stupa way of celebrating a special day [Available at <http://icestupa.org/news/ice-stupa-way-of-celebrating-a-special-day6th-of-ju>, accessed
383 2019-10-01]
- 384 Wangchuk, S. (2015e). World water day at ice stupa [Available at <http://icestupa.org/news/world-water-day-at-ice-stupa>, accessed 2019-10-01]
- 385 WMO (2018). *Guide to Instruments and Methods of Observation* (World Meteorological Organization ;
386 2018 (2018 Edition))
- 387 Woolf, H. M. (1968). *On the Computation of Solar Elevation Angles and the determination of sunrise and
388 sunset times* (National Aeronautics and Space Administration)
- 389 Zhou, S., Kang, S., Gao, T., and Zhang, G. (2010). Response of zhadang glacier runoff in nam co basin,
390 tibet, to changes in air temperature and precipitation form. *Chinese Science Bulletin* 55, 2103–2110.
391 doi:10.1007/s11434-010-3290-5